5th Joint International Symposium on Deformation Monitoring (JISDM), 20-22 June 2022, Valencia, Spain
DOI: http://doi.org/10.4995/JISDM2022.2022.13816

Two-epoch TLS deformation analysis of a double curved wooden structure using approximating B-spline surfaces and fully-populated synthetic covariance matrices

Gabriel Kerekes[1], Jakob Raschhofer[2], Corinna Harmening[2] ,Hans Neuner[2], Volker Schwieger[1]

[1] Institute of Engineering Geodesy, University of Stuttgart, Geschwister-Scholl-Str. 24D, 70174 Stuttgart, Germany, (gabriel.kerekes@iigs.uni-stuttgart.de; volker.schwieger@iigs.uni-stuttgart.de)
[2] Department of Geodesy and Geoinformation, TU Wien, Wiedner Hauptstr. 8/E120, 1040 Vienna, Austria, (jakob.raschhofer@geo.tuwien.ac.at; corinna.harmening@geo.tuwien.ac.at; hans.neuner@geo.tuwien.ac.at)

Key words: *B-spline surfaces; deformation analysis; hypothesis tests; laser scanning; point clouds; synthetic variance-covariance matrix*

ABSTRACT

This contribution presents a B-spline-based approach of area-wise deformation analysis applied on elements of a double curved wooden tower. The monitored object is the Urbach Tower with a height of 14 m. Terrestrial laser scans from two epochs acquired under real-world conditions are used for approximating two jointly parametrized B-spline surfaces of the tower's outer shell. The stochastic model of the observations used within the surface approximation is based on elementary error theory and is defined by a synthetic variance-covariance matrix (SVCM). In addition to previous work on this topic, the object's dimension is extended from a few dm to a few m and the measurement distance ranges from 20 to 60 m. Moreover, environment specific error sources are addressed in the SVCM, revealing the effect of the object's dimension as well as of additional elementary errors on the estimated B-spline surfaces and the subsequent deformation analysis. Based on constructed points pairs using a grid of surface parameters, rigid body movements of the object under investigation are estimated while at the same time distorted regions of the wooden tower are detected. All results of the deformation analysis are statistically verified using hypothesis tests based on the elementary error model propagated through the processing algorithms of surface estimation and deformation analysis. The results demonstrate that during the modelling and deformation analysis, the measurement noise is reduced and therefore distorted regions are detectable in a statistically correct way.

I. Introduction

Area-wise deformation analysis has become a trend in the past 20 years, yet there is no general accepted workflow or method for conducting it (*cf.* Neuner *et al.*, 2016; Wunderlich *et al.*, 2016). Point clouds of natural or artificial object acquired by Terrestrial Laser Scanning (TLS) are in most cases simply compared to one another (Holst *et al.*, 2017). Popular open-source software like Cloud Compare (Girardeau-Montaut, 2019) offer tools for quick geometrical comparisons. However, typically in geodetic deformation analysis (Heunecke and Welsch, 2000) the estimated geometric changes, have to be assessed by statistical tests.

The current contribution presents an approach to area-wise deformation analysis for two epochs based on estimated B-Spline surfaces. The stochastic model of the TLS observations is defined by a synthetic variance-covariance matrix (SVCM) which contains the instrument related errors and environment related errors. The workflow is applied to a part of a double curved 14 m high wooden structure, called the Urbach Tower. This approach continues the work of Raschhofer *et al.* (2021) by extending the analysis to object dimension of several meters as well as to measurement distances of tenth of meters. This implies including the atmospheric conditions in the SVCM, applying a different instrumental error model and using a different source of reference data. Additionally, this paper also focuses on deformation analysis. In contrast to other publications on similar topics (*cf.* Paffenholz and Wujanz, 2019; Kermarrec *et al.*, 2019), point pairs of the estimated B-splines in two epochs are constructed and rigid body movements are estimated while simultaneously distorted regions are detected.

In Section II, the new methods are presented and the theoretical background is briefly given. The experimental setup and deformation analysis are shown in Section III, while Section IV concludes this contribution.

II. Methods - Deformation analysis

A. *Estimation of rigid body movements and simultaneous localisation of non-distorted regions using sampled approximating B-spline surfaces*

In this contribution the approach of Harmening *et al.*, (2021) is followed, which is based on B-spline models of epoch-wise acquired point clouds. Corresponding points in different epochs are constructed using

identical surface parameters on the different, epoch-related B-spline surface. These corresponding points, resulting from the discretizations of the B-spline surfaces, are used to robustly estimate rigid body movements and to initially define non-distorted regions of the object. Finally, the non-distorted regions are extended and their stability as well as their extents are statistically confirmed. The individual steps of this algorithm are explained in the following sections.

1) Estimation of B-spline surfaces for deformation analysis: A B-spline surface is usually defined by (Piegl and Tiller, 1997; Bureick *et al.*, 2016) (Eq. 1):

$$\widehat{\boldsymbol{S}}(u,v) = \sum_{i=0}^{n}\sum_{j=0}^{m} N_{i,p}(u)\, N_{j,\mathrm{q}}(v)\, \boldsymbol{P}_{i,j} \qquad (1)$$

A three-dimensional surface point $\widehat{\boldsymbol{S}}(u,v)$ in Cartesian coordinates is expressed as the weighted average of the $(n+1)\times(m+1)$ control points $\boldsymbol{P}_{i,j}$. The corresponding weights are the functional values of the B-spline basis functions of degree p and q $N_{i,p}(u)$ and $N_{j,\mathrm{q}}(v)$ which can be recursively computed (*cf.* Cox, 1972; De Boor, 1972). The B-spline's domain is split into knot spans by two knot vectors $\boldsymbol{U} = [u_0, \dots, u_r]$ and $\boldsymbol{V} = [v_0, \dots, v_s]$, which are defined in direction of the surface parameters.

Before estimating the control points of the best-fitting B-spline surface, the measurements have to be located on the surface to be estimated. This is achieved by allocating them convenient surface parameters u and v (*cf.* Harmening and Neuner, 2015). Using these surface parameters, the knot vectors can also be estimated (Piegl and Tiller, 1997; Schmitt and Neuner, 2015; Bureick, 2020).

The choice of the appropriate number of control points (Harmening and Neuner, 2017) is usually specified a priori and cubic B-splines ($p = q = 3$) are generally accepted.

When B-spline surfaces are used as a basis for deformation analysis, a joint parametrization is essential (*cf.* Harmening and Neuner, 2017). The projection of the measured point clouds onto a joint base surface and the use of its knot vectors make this approximately possible.

2) Constructing point pairs on approximating B-spline surfaces: By means of a regular grid of surface parameters, points $\widehat{\boldsymbol{S}}(u,v)$ (*cf.* Equation 1) are calculated on the B-spline surfaces estimated in each epoch.

These calculated points are treated as corresponding three-dimensional surface points. The VCM of the estimated control points is propagated for the constructed surface points.

In order to achieve a detailed statement regarding the position and extent of the distortions, the number of sampled surface points μ should considerably exceed the number of control points (Hobmaier, 2020). This, on the other hand, leads to singularities in the corresponding variance covariance matrix. The occurring singularities are handled using the pseudoinverse.

3) Identification of stable regions for the determination of approximate values of the elements of rigid body movements: Based on point pairs between epochs, the elements of the rigid body movements are determined, at first approximately. The required parameters of the rigid body movement are estimated by means of a three-dimensional similarity transformation (Heunecke *et al.*, 2013).

Unfortunately, it cannot be assumed that the object under investigation is subjected only to rigid body movements. Additional object distortions bias the estimated transformation parameters (Harmening *et al.*, 2021). Thus, the estimation of rigid body movements needs to be relay only on corresponding point pairs on the B-spline surfaces that are not subjected to distortions.

The iterative random sample consensus (RANSAC)-algorithm (Fischler and Bolles, 1981) is a suitable methodological tool enabling the identification of similarity transformation.

The basic principle of RANSAC is to firstly select randomly the minimal possible subset from a set of the maximum available corresponding points, which uniquely determines the model's parameters.

All corresponding surface points from the epoch 0 are transformed using the estimated parameters of the preliminary model. The Euclidean distance d_k $(k = 0, \dots, \mu - 1)$ between each transformed point belonging to epoch 0 and its corresponding point in epoch 1 provides the measure for including the corresponding points into the consensus set of model-conforming points. The distance is compared to the error tolerance. The latter is assessed individually using the τ-fold standard deviations of the calculated distances $\sigma_{k,d}$. When (Eq. 2)

$$d_k \leq \tau\sigma_{d,k} \qquad (2)$$

is fulfilled, the corresponding point pair is assigned to the consensus set. If the number of points satisfying Equation 2 is below a certain minimum number, another RANSAC-iteration is performed. Caspary, (2013) and Harmening *et al.* (2021) provide approaches to select freely definable parameters (factor τ, maximum number of iterations, minimum number of model-compliant points n_{min}) of this algorithm.

Provided that the amount of model-compliant points is larger than n_{min}, the model-compliant points are used to estimate the parameters of the similarity transformation in an over-determined extended model.

4) Statistically Based Localization of Distortions: Usually, the consensus set does not cover the entire non-distorted region of the B-spline surface. Therefore, the consensus set is extended using hypotheses tests of individual point pairs (starting with the point pair that has the smallest distance), which are not assigned to the consensus set (Harmening *et al.*, 2021). Based on this extension, the parameters of the rigid body movement are re-estimated. A final global test is used to check the consistency of non-distorted point pairs (Harmening *et al.*, 2021).

III. Case Study Urbach Tower

A. *Experimental set-up*

The monitored object is a unique curved wooden 14 m tall structure, called the Urbach Tower (Figure 1). It was built in 2018 using new self-shaping processes for the curved wooden components and constitutes the first structure worldwide made from self-shaped building-scale components (ICD, 2019). Due to this, it is considered a challenging object for area-wise deformation analysis.

Figure 1. The Urbach Tower (ICD, 2019).

The tower was scanned in two epochs with a Riegl VZ2000 scanner from three different station points. The scanning positions were chosen to capture the front part of the tower from a single station point and were located at distances of 20 m, 40 m and 60 m from the tower. Additionally, the weather parameters air temperature and air pressure were recorded for both campaigns in the area of interest. This was done with a handheld precision Thermo-Barometer, Greisinger GTD1100 approximately at the instrument height (*e.g.* 1.8 m above ground). Figure 2 gives an overview of the on-site situation. In order to create a common geodetic datum for both epochs, fixed points were marked in the spring of 2020 before the actual measurement campaigns.

The tower is in the middle of a field and there are not many choices for stable areas with favourable geometric distribution of the network points. Nevertheless, five network points were initially marked around the tower and the planned TLS station points. Three points were marked with concrete dowels in the tower base and the nearby bench foundation, one with wooden dowel in a wooden electricity pole and the other with an 80 cm aluminium peg near the access road. All points assure the same mechanical centre between different TLS target types and reflectors.

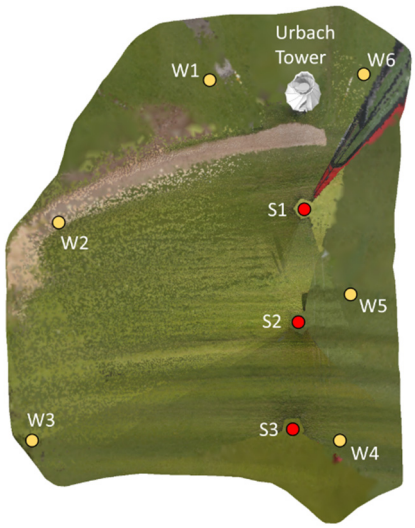

Figure 2. Overview of TLS station points (Sx) and weather points (Wx) relative to the Urbach tower.

In both epochs all network points were measured with a 0.5" Leica TS30 Total Station (TS) to verify whether the reference point are stable. After a deformation analysis (congruence test), no significant differences (α=5%) were identified. Therefore, the coordinates of the reference network can be used for the TLS point cloud transformation without inducing errors due to different datums.

In each epoch, additional to the mentioned TLS scans, reference scans with a high precision close range scanner were made for several wooden plates. The Surphaser 100 HSX-SR was used due to its very low range noise <1 mm up to 4 m (Basis Software Inc., 2021). With a recommended working range of 1-7 m, the common points used for georeferencing are the points placed near the tower. The working range was also the restriction for the analysed part of the tower, as later explained (*cf.* Section III).

B. *Stochastic model*

The stochastic model used to describe the TLS observations' uncertainty is established based on the elementary error theory. Specifically, the model is represented by a synthetic variance-covariance matrix (SVCM) constructed as explained in Kauker and Schwieger (2017), Kerekes and Schwieger (2020) and Raschhofer *et al.* (2021). Without resuming the theory of defining fully populated VCM $\Sigma_{ll}^{(\lambda\theta R)}$ in observation space or the equivalent $\Sigma_{ll}^{(xyz)}$ in coordinate space, only

the relevant different aspects to the aforementioned publications are highlighted.

As before, errors are grouped in three classes according to their correlation nature: non-correlating, functional correlating and stochastic correlating errors. All three classes are represented as follows:

1. Non-correlating errors: angle noise (λ –horizontal and θ - vertical) and range noise;
2. Functional correlating errors: calibration parameters of the hybrid TLS (a to c in Table 1);
3. Stochastic correlating errors: air temperature; air pressure and temperature gradient.

Starting values for the first two groups of non-correlating and functional correlating errors (Table 1) have been taken from the TLS technical specifications (*cf.* Riegl Laser Measurement Systems GmbH, 2021) and from available literature.

Table 1. Parameters of non-correlating and functional correlating errors (Riegl)

Type of error	Parameter	Standard deviation
Non-correlating errors	Range noise [mm]	5
	Angle noise [mgon]	λ = 0.55
		θ = 1.66
Functional correlating errors	a0 [mm]	0.34
	a1 [ppm]	40
	b4 [mgon]	3.18
	b6 [mgon]	1.91
	c0 [mgon]	1.08
	c1 [mgon]	1.85
	c4 [mgon]	0.64

An explanation of the parameters and their role in the functional mode is given in Kerekes and Schwieger (2020).

As for the stochastic correlating errors, a slightly improved approach is used (*cf.* Kerekes and Schwieger 2020). The covariances of the environmental elementary errors are not determined based on general correlation coefficients. In Kerekes and Schwieger (2020) section 3, this was done between the lowest and highest observation line of the spatial Vertical Gradient Temperature (VGT) model. Now it is possible to have specific values for covariances of air temperature, air pressure and vertical temperature gradient among observations between scanner and the scanned object. A prerequisite is a digital terrain model (DTM) and measurement for some of the meteorological parameters in the area (*cf.* Figure 2). An example for one epoch is given in Figure 3. The different values of air temperature obtained for the interpolated points and DTM are presented in different colours according to the temperature scale. As observed, within this small areal temperature differences are within less than 3°C. It is also mentioned that these values are not used to correct the observations, since this is not of interest in this contribution.

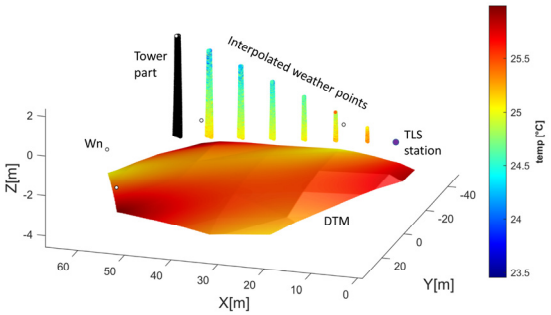

Figure 3. Example of how variance and covariance are determined for each observation based on environmental errors and interpolated points.

This resembles measurement set-ups used in permanent laser scanning for monitoring (Kuschnerus *et al.*, 2021) that are recently receiving increased importance.

Another important elementary error group constitutes the object surface properties, but this is not treated in this contribution.

C. *Constructing Corresponding Surface Points*

The lower part of the tower façade with a height of 5m was used for the analysis, due to the good spatial precision ($0.35\ mm \leq \sigma_{xyz} \leq 0.70\ mm$; Helmert's point error) assumed in this region using the reference Surphaser laser scanner. The resulting point cloud of the first epoch and subsequently the estimated B-spline surface using the identity matrix as stochastic model serve as reference surface. Since this surface is only used as reference surface and no functional correlating errors are known for the Surphaser scanner, the identity matrix is used here. As seen in Raschhofer *et al.* (2021), the differences of estimated control points position for an estimated surface at close range (section 4.1. in aforementioned publication) using identity, diagonal or fully populated matrix as a stochastic model are negligible. Since no stochastic information is needed for the projection, the identity matrix is chosen for simplicity.

To ensure a joint B-spline parameterization, the Riegl point clouds of both epochs are projected onto this reference surface to obtain surface parameters. Furthermore, the number of control points and the knot vectors are likewise used for the estimation.

As for the stochastic model, a SVCM is introduced into the estimation. For each point cloud, the SVCM is adjusted by varying the standard deviations of the non-correlating errors, as performed in Raschhofer *et al.*, (2021), so that the null hypothesis of the global test of the individual B-spline surface estimation cannot rejected. Table 2 shows the values obtained for the standard deviations of the non-correlating errors.

The applied noise standard deviations differ between epochs due to the missing consideration of object surface properties in the SVCM and of the inter-epochal correlations. The tower outer appearance visibility changed between the epochs, varying from birch

natural light yellow colour to light grey. The other elementary errors types in the SVCM (instrumental and environmental group) have not been modified.

Table 2. Explicit standard deviations for non-correlating errors (Riegl scans E0: epoch 0; E1: epoch 1; S: station points)

Parameter	S1 E0	S1 E1	S2 E0	S2 E1	S3 E0	S3 E1
Range noise [mm]	5	5	5	5	5	5
Angle noise (λ) [mgon]	5	6.1	2.5	2.8	2.2	2.7
Angle noise (θ) [mgon]	15	18.3	7.5	8.7	6.5	8.3

The epoch-wise estimated approximating B-spline surfaces are discretised as described in Section II A 2. Table 3 shows the different levels of discretisation chosen, where $n_{u,v}$ indicates the number of points in the respective parameter direction.

Table 3. Overview of the discretization

Discretisation	$n_u * n_v$
V1	$20 * 15$
V2	$30 * 20$

The boundary regions of the estimated surfaces are estimated less accurately than the inner regions (Hobmaier, 2020). To avoid distortions in the deformation analysis caused by boundary points, the surfaces are discretised with surface parameters (u, v) in the interval $[0.05, 0.95]$. In the inner regions of the surfaces, the discretised points obtain a homogeneous level of accuracy.

D. *Detecting Non-Distorted and Distorted Regions*

The result of the RANSAC method described in Section II A strongly depends on the freely chosen parameters, especially the parameters τ and the minimum number of model-compliant points n_{min} (Harmening and Neuner, 2016). The influence of these parameters on the number of iterations $\#i$ and the number of point pairs in the consensus set n_{cs} is shown in Table 4 for the respective station point and discretization. The aim of trying different combinations of τ and n_{min} is to obtain a relatively high amount of points in n_{cs}. If n_{min} is chosen to high, the maximum amount of iterations exceeds. It is mentioned that only the parameters of the respective best results are given.

Table 4. Influence of selected RANSAC parameters

Discretization	τ	n_{min}	$\#i$	n_{cs}
S1 - V1	2	22	2	184
S2 - V1	1	22	12	154
S3 - V1	2	22	647	77
S1 - V2	2	22	4	224
S2 - V2	2	22	41	167
S3 - V2	3	32	836	144

Values of $\tau > 3$ were not considered with regard to the 3σ-rule (Heuneke *et al.*, 2013).

Using data set S3-V1, a large number of iterations $\#i$ is needed to find a comparatively small amount of point pairs in the consensus set n_{cs}. Although the choice of $\tau = 3$ increases the error threshold (*cf.* Equation 2), similar behaviour is also observed for the data set S3-V2.

The focus in this contribution is on detecting distorted regions, since no large rigid-body movement of the tower is expected. The parameters of the similarity transformation are mainly intended to eliminate the residual misclosures from the georeferencing and, thus, are not discussed further.

An interpretation of the correctness of the following results presented is discussed in Section IV based on the reference result obtained with the Surphaser.

Using data set S1-V1, the results of the deformation analysis are shown in Figure 4. For the circled points, the null hypothesis (Eq. 3)

$$H_0: E(\widehat{\boldsymbol{\nabla}}) = 0 \tag{3}$$

stating that a certain point belongs to the consensus set, has to be rejected. It is therefore examined whether the estimated gross errors $\widehat{\boldsymbol{\nabla}}$ differ significantly from the nominal value $\widehat{\boldsymbol{\nabla}} = 0$. Thus, these points are assumed to lie in the distorted region.

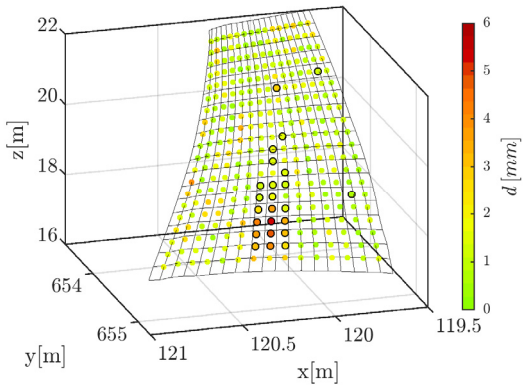

Figure 4. Distorted regions using data set S1-V1.

The result (see Figure 5) of the deformation analysis of data set S2-V1 supports the result of S1-V1.

The regions with deformations of 6 mm (see bottom centre) are detected from the different data sets. The occurrence of type I errors cannot be completely avoided, although a high confidence probabilit y of $1 - \alpha$ ($\alpha = 3\%$) is chosen. Since type I errors usually do not occur in groups, most of them can be identified by investigating their direct neighbourhood. If their entire neighbourhood is located in the non-distorted region, it can be assumed that a type I error exists (Harmening *et al.*, 2021).

Figure 6 shows results of the deformation analysis with discretization V2 of the station points S2. A comparable result is also achieved using the S1-V2 data set.

The regions with large deformation agree with the results using data sets V1. However, there is a

noticeable increase of distorted regions using a denser discretization. In Figure 6, points with larger distances than others, which are classified to the distorted regions, are obviously included in the stable point set, especially in the upper area.

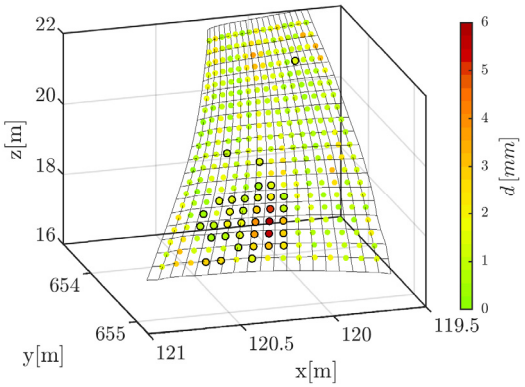

Figure 5. Distorted regions using data set S2-V1.

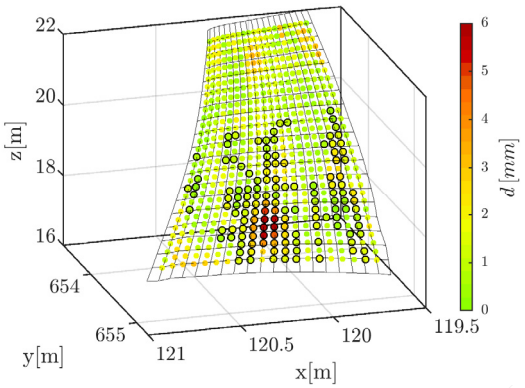

Figure 6. Distorted regions using data set S2-V2.

In order to investigate this behaviour, Figure 7 shows the initial stable point set (the upper region) of the data set S2-V2 obtained after applying RANSAC. Hobmaier, (2020) states that a dependency of the initial stable point set according to the RANSAC or the order of the individual tests occurs in the case of a test decision of a point. Thus, points that are initially part of the consensus set are more likely to be accepted as non-distorted than points that are not initially included. A comparison of Figure 6. and Figure 7. reinforces this thesis. The initial consensus set, hence, plays an essential role in the outcome of a deformation analysis.

The deformation analysis using the data sets of S3 also detects the largest deformations. However, there is a comparatively high number of deformed points observed over the entire surface. This can be explained due to the georeferencing of this station point with an accuracy up to $14\ mm$, which causes falsification of the joint B-spline parameterization. This leads to possible falsified distances, which play a major role in deformation analysis. (Harmening and Neuner, 2017) point out that reasonable comparison is only possible if the B-spline surfaces are based on the same parameterization.

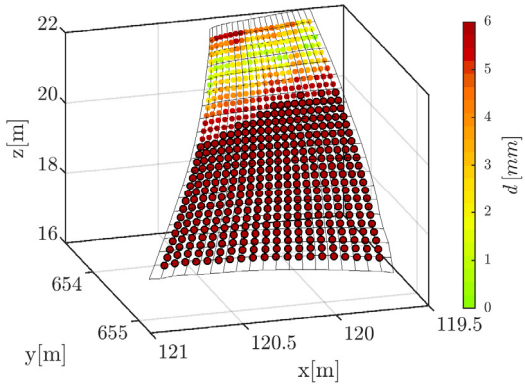

Figure 7. Initial solution (points without black circle) after RANSAC using data set S2-V2.

IV. Validation and Evaluation

The aforementioned results are verified by a comparison with the Surphaser point clouds. For this purpose, a deformation analysis with a sampling-resolution V1 (*cf.* Table 3) of the Surphaser B-spline surfaces of both epochs is performed. It should be noted that the stochastic model $\Sigma_{ll}^{(\lambda\theta R)}$ of the observations in the estimation process is only filled with values of range noise $\sigma_R = 0.3\ mm$ and angle noise $\sigma_{\lambda,\theta} = 4.6\ mgon$ (Basis Software Inc., 2021). Due to the lack of knowledge concerning functional correlating errors, no correlations are taken into account here. The values of the noise are slightly adjusted in such a way that the global test of the approximation model is passed. The selected RANSAC parameters are $\tau = 2$ and $n_{min} = 32$. This results in $\#i = 17$ and $n_{cs} = 187$. Figure 8 shows the distorted regions detected using the Surphaser point clouds.

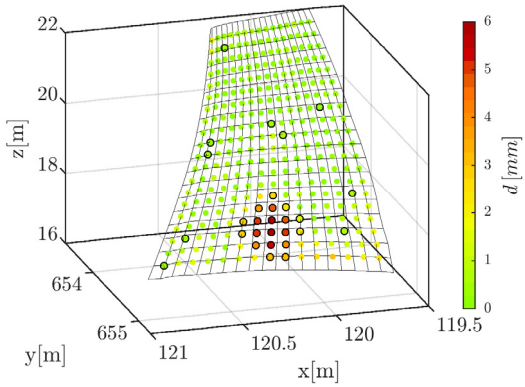

Figure 8. Distorted regions - Surphaser V1.

Comparing Figure 8 with the results in Section III.D it can be seen that the regions of deformation (max. $6\ mm$) are successfully detected from all data sets used. Keeping in mind that the range noise of the Riegl scanner alone is around $5\ mm$, a large extent of the measurement noise is reduced during the deformation analysis using B-spline surfaces.

Even with the deformation analysis using the data of the Surphaser, errors of type I cannot be completely avoided.

The comparison illustrates that even with the worse precisions values of the Riegl scanner in comparison to the Surphaser scanner (especially in range noise *cf.* Table 2), realistic results are achieved using the deformation analysis.

The advantage of including a fully populated SVCM in a deformations analysis is reinforced by a comparison with the outcomes of a deformation analysis, which uses a diagonal matrix as a stochastic model for the observations of the Riegl scans. In the latter, the observations are weighted in such a way that the global test of the approximation model is passed. Figure 9 shows the result of the data set S2-V1 using a diagonal matrix instead of the SVCM. It can be seen that many points are identified as significantly deformed (black circles), outside the deformed area indicated by the Surphaser data. Obviously, the inclusion of appropriate variances and covariances from the fully populated SVCM (*cf.* Figure 5) improves the result, especially with regard to the distribution of points detected as distorted with respect to lowering type I errors.

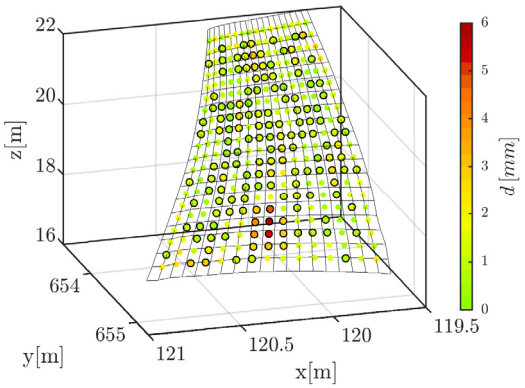

Figure 9. Distorted regions using data set S2-V2; stochastic model diagonal matrix as VCM.

From these findings, it can be assumed that a fully populated SVCM leads to an improvement also for the Surphaser data. Hence, realistic covariances play an essential role in the context of the deformation analysis presented using real TLS measurements.

V. Conclusion

This paper introduces a strategy that allows for estimating rigid body movements and detection of distorted regions at the same time, using best-fit B-spline surfaces. The stochastic properties of the point clouds are described by fully populated SVCMs in the estimation of the B-spline surface.

The results demonstrate that during the modelling and deformation analysis, the measurement noise is reduced and therefore distorted regions are detectable in a statistically sound way.

As noticed for the station S3, a common surface parameterization in both epochs is important for the realistic deformations analysis.

Furthermore, a comparison of the results of the deformation analysis using different stochastic models for the observations illustrates the advantages of including appropriate stochastic models in form of a SVCM in the B-spline estimation.

VI. Acknowledgements

This research was partly funded by the DFG (German Research Foundation), SCHW 838/7-3 within the project IMKAD II “Integrated space-time modelling based on correlated measurements for the determination of survey configurations and the description of deformation processes”. The other funding party of IMKAD II (I3869) was the Austrian Science Fund (FWF). The authors express their gratitude to the DFG and the FWF for funding this project. The project was also an associated project (AP 07) with the Cluster of Excellence Integrative Computational Design and Construction for Architecture (IntCDC) partially supported by the DFG under Germany’s Excellence Strategy—EXC 2120/1—390831618.

References

Basic Software Inc. (2021). *Data sheet Surphaser 3D Laser Scanners.* Available at: https://www.surphaser.com/pdf/Surphaser%20100HSX.pdf, last accessed 10.11.2021.

Bureick, J., Neuner, H., Harmening, C. and Neumann, I. (2016). Curve and surface approximation of 3D point clouds. *Allgemeine Vermessungsnachrichten*, Vol. 123, No. 11-12.

Bureick, J. (2020). *Robuste Approximation von Laserscan-Profilen mit B-Spline-Kurven*. PhD Thesis, University of Hannover. Verlag der Bayerischen Akademie der Wissenschaften (eds.), DGK-C 852, Munich.

Caspary, W. (2013). *Fehlertolerante Auswertung von Messdaten: Daten- und Modellanalyse, robuste Schätzung*. De Gruyter, New York.

Cox, M.G. (1972). The Numerical Evaluation of B-Splines. *IMA Journal of Applied Mathematics*, Vol. 10, No. 2.

De Boor, C. (1972). On calculating with B-splines. *Journal of Approximation Theory*, Vol. 6, No. 1.

Fischler, M.A. and Bolles, R.C. (1981). Random sample consensus: A paradigm for model fitting with applications to image analysis and automated cartography. *Communications of the ACM*, Vol. 24, No. 6.

Girardeau-Montaut, D. (2019) Point processing with Cloud Compare, In: *Proc. of Point Cloud Processing Workshop 2019 Stuttgart*. Available at: pcp2019.ifp.uni-stuttgart.de/presentations/04-CloudCompare_PCP_2019_public.pdf, last accessed 24.01.2020.

Harmening, C., Hobmaier, C. and Neuner, H. (2021). Laser Scanner–Based Deformation Analysis Using Approximating B-Spline Surfaces. *Remote Sensing*, Vol. 13, No. 18.

Harmening, C. and Neuner, H. (2015). A constraint-based parameterization technique for B-spline surfaces. *Journal of Applied Geodesy*, Vol. 9, No. 3.

Harmening, C. and Neuner, H. (2016). Detecting rigid body movements from TLS-based areal deformation measurements. In: *Proc. of the FIG Working Week 2016*, FIG Christchurch, New Zealand.

Harmening, C. and Neuner, H. (2017). Choosing the Optimal Number of B-spline Control Points (Part 2: Approximation of Surfaces and Applications). *Journal of Applied Geodesy*, Vol. 11, No. 1.

Heunecke, O., Kuhlmann, H., Welsch, W., Eichhorn, A. and Neuner, H. (2013) (eds). *Auswertung Geodätischer Überwachungsmessungen - Handbuch Ingenieurgeodäsie* 2nd ed., Wichmann, Berlin.

Heunecke, O., and Welsch, W.M. (2000). Models and Terminology for the Analysis of Geodetic Monitoring Observations. *Official Report of the Ad-Hoc Committee of FIG Working Group 6.1*.

Hobmaier, C. (2020). *Flächenhafte Deformationsanalyse unter Verwendung von approximierenden B-Spline-Flächen*. Master's Thesis. Technical University of Vienna - Department für Geodäsie und Geoinformation/Ingenieurgeodäsie.

Holst, C., Klingbeil, L., Esser, F. and Kuhlmann, H. (2017). Using point cloud comparisons for revealing deformations of natural and artificial objects. In: *Proc. of INGEO 2017, 7th International Conference on Engineering Surveying*. Kopáčik, A., Kyrinovič, P., Henriques, M.J. (eds), Lisabon.

ICD (2019). *Urbach Tower, Institute for Computational Design and Construction, University of Stuttgart*. Available at: https://www.icd.uni-stuttgart.de/projects/remstal-gartenschau-2019-urbach-turm/, last accessed 29.10. 2021.

Kauker, S. and Schwieger, V. (2017). A synthetic covariance matrix for monitoring by terrestrial laser scanning. *Journal of Applied Geodesy*, Vol. 11, No. 2.

Kerekes, G. and Schwieger, V. (2020). Elementary Error Model Applied to Terrestrial Laser Scanning Measurements: Study Case Arch Dam Kops. *Mathematics*, Vol. 8, No. 4.

Kermarrec, G., Alkhatib, H. and Paffenholz, J.-A. (2019). Original 3D-Punktwolken oder Approximation mit B-Splines: Verformungsanalyse mit CloudCompare. In: *Proc. of GeoMonitoring 2019*, online available at: https://www.repo.uni-hannover.de/handle/123456789/4549.

Kuschnerus, M., Schröder, D. and Lindenbergh, R. (2021). Environmental Influences on the Stability of a Permanently Installed Laser Scanner. *The International Archives of the Photogrammetry, Remote Sensing and Spatial Information Sciences*, Vol. XLIII-B2-2021.

Neuner, H., Holst, C. and Kuhlmann, H. (2016). Overview on Current Modelling Strategies of Point Clouds for Deformation Analysis. *Allgemeine Vermessungsnachrichten*, Vol. 123, No. 11-12.

Paffenholz, J.-A. and Wujanz, D. (2019). Spatio-temporal monitoring of a bridge based on 3D point clouds - A comparison among several deformation measurement approaches. In: *Proc. of 4th Joint International Symposium on Deformation Monitoring (JISDM)*.

Piegl, L. and Tiller, W. (1997). *The NURBS Book*. 2nd ed. Springer Berlin/Heidelberg.

Raschhofer, J., Kerekes, G., Harmening, C., Neuner, H. and Schwieger, V. (2021). Estimating Control Points for B-Spline Surfaces Using Fully Populated Synthetic Variance–Covariance Matrices for TLS Point Clouds. *Remote Sensing*, Vol. 13, No. 16.